CHEMICAL PHYSICS

Verwey-type charge ordering transition in an open-shell *p*-electron compound

Peter Adler,[1] Peter Jeglič,[2] Manfred Reehuis,[3] Matthias Geiß,[4] Patrick Merz,[1] Tilen Knaflič,[2] Matej Komelj,[2] Andreas Hoser,[3] Annette Sans,[1,5] Jürgen Janek,[4] Denis Arčon,[2,6]* Martin Jansen,[1,5]* Claudia Felser[1]

The Verwey transition in Fe_3O_4, a complex structural phase transition concomitant with a jump in electrical conductivity by two orders of magnitude, has been a benchmark for charge ordering (CO) phenomena in mixed-valence transition metal materials. CO is of central importance, because it frequently competes with functional properties such as superconductivity or metallic ferromagnetism. However, the CO state in Fe_3O_4 turned out to be complex, and the mechanism of the Verwey transition remains controversial. We demonstrate an archetypical Verwey-type transition in an open *p*-shell anionic mixed-valence compound using complementary diffraction and spectroscopic techniques. In Cs_4O_6, a phase change from a cubic structure with a single crystallographic site for the molecular O_2^{x-} building units to a tetragonal structure with ordered superoxide O_2^- and peroxide O_2^{2-} entities is accompanied by a drastic drop in electronic conductivity and molecular charge fluctuation rates. The simple CO pattern of molecular units and the lack of magnetic order suggest Cs_4O_6 as a model system for disentangling the complex interplay of charge, lattice, orbital, and spin degrees of freedom in Verwey-type CO processes.

INTRODUCTION

The phenomenon of charge ordering (CO) in mixed-valence compounds (*1*) is closely linked to some of the most important material's features in the solid state, including the Verwey transition in magnetite (Fe_3O_4) (*2*–*6*), dramatic changes of electrical conductivity with colossal magnetoresistance effects in manganites (*7*–*9*), the competition between charge order and high-temperature superconductivity in layered cuprates (*10*, *11*), and electron Wigner crystallization in quasi one-dimensional cuprates (*12*). The common thread to all these phenomena is that the mixed-valence states and CO are based on 3*d* electrons of transition metal ions. The Verwey transition in magnetite, Fe_3O_4, which undergoes a structural phase change with a concomitant jump in electrical conductivity at T_V = 125 K (*2*), has been intensely studied as a model case for CO phenomena. However, the validity of Verwey's original model of Fe_3O_4 relying on a CO of Fe^{2+} and Fe^{3+} ions at T_V (*3*) has been challenged (*4*, *5*), and the CO pattern turned out to be more complex, involving the formation of so-called trimerons (*6*). In a generalized sense, the Verwey transition has been defined as a "spontaneous intercorrelated change of both lattice symmetry and electric conductivity in certain ionic crystals" (*4*).

Recently, the commonalities between the strongly correlated transition metal compounds and molecular solids containing open-shell oxygen O_2^- anions found interest (*13*–*22*). Whereas in superoxides with merely O_2^- units low-dimensional magnetic order driven by orbital order has been established (*19*), alkali sesquioxides A_4O_6 (A = Rb, Cs) stand out as unique representatives of *p*-electron molecular solids with mixed-valence states of dioxygen anions (*23*, *24*). Four electrons donated by the respective alkali metal ions are shared among three O_2 units, thus formally implying the chemical formula $A_4(O_2^{2-})(O_2^-)_2$ with diamagnetic peroxide (O_2^{2-}) and paramagnetic superoxide (O_2^-) anions. However, in the long-known cubic (C) crystal structure of A_4O_6 (*23*–*25*), all dioxygen anions are crystallographically equivalent, which requires that the fourth electron is delocalized among the three anionic units. A recent report on a tetragonal (T) phase in Rb_4O_6 single crystals (*26*) hints at a possible charge-ordered ground state in A_4O_6 mixed-valence compounds. Using diffraction and spectroscopic probes, here, we demonstrate that the sister compound Cs_4O_6 undergoes an archetypical Verwey-type CO transition bearing many of the characteristics of Verwey's original model. Moreover, the molecular and the *p*-electron nature of the basic O_2^{x-} building units disclose the importance of orbital physics for the Verwey-type CO transition and offer new possibilities for exploring the coupling between entangled degrees of freedom.

RESULTS

The structural properties of Cs_4O_6 were investigated by powder neutron diffraction (PND) (see Fig. 1 and table S1). Rietveld refinement of a PND pattern taken at 375 K reveals the known C structure (*23*, *24*), where individual O–O bonds of O_2 units are directed along the three crystallographic axes. In this average structure, all dioxygen anion entities have apparently identical O–O bond lengths. At slow cooling, Cs_4O_6 undergoes a phase transition near 260 K, acquiring the structure of the T modification of Rb_4O_6 (*26*). In the T structure of Cs_4O_6, substantially different O–O bond distances of 1.53 and 1.31 Å evidence a fully charge-ordered arrangement of O_2^{2-} and O_2^- anions. The O_2^{2-} units have their O–O bonds aligned precisely along the crystallographic *c* axis, whereas the O–O bonds of the open-shell O_2^- units tilt at an angle of 17° relative to the T *c* axis. Accordingly, the structural transformation from the C into the T phase involves a large-amplitude molecular reorientation, where interatomic distances change significantly (table S2). The 2 K pattern of the T phase does not reveal any magnetic Bragg intensity, which indicates the absence of long-range magnetic order. This is consistent with the temperature dependence of the

[1]Max Planck Institute for Chemical Physics of Solids, Nöthnitzer Straße 40, 01187 Dresden, Germany. [2]Jožef Stefan Institute, Jamova c. 39, 1000 Ljubljana, Slovenia. [3]Helmholtz-Zentrum Berlin für Materialien und Energie, 14109 Berlin, Germany. [4]Institute of Physical Chemistry and Center for Materials Research, Justus-Liebig-University Giessen, Heinrich-Buff-Ring 17, 35392 Giessen, Germany. [5]Max Planck Institute for Solid State Research, Heisenbergstr. 1, 70569 Stuttgart, Germany. [6]Faculty of Mathematics and Physics, University of Ljubljana, Jadranska c. 19, 1000 Ljubljana, Slovenia.
*Corresponding author. Email: denis.arcon@ijs.si (D.A.); m.jansen@fkf.mpg.de (M.J.)

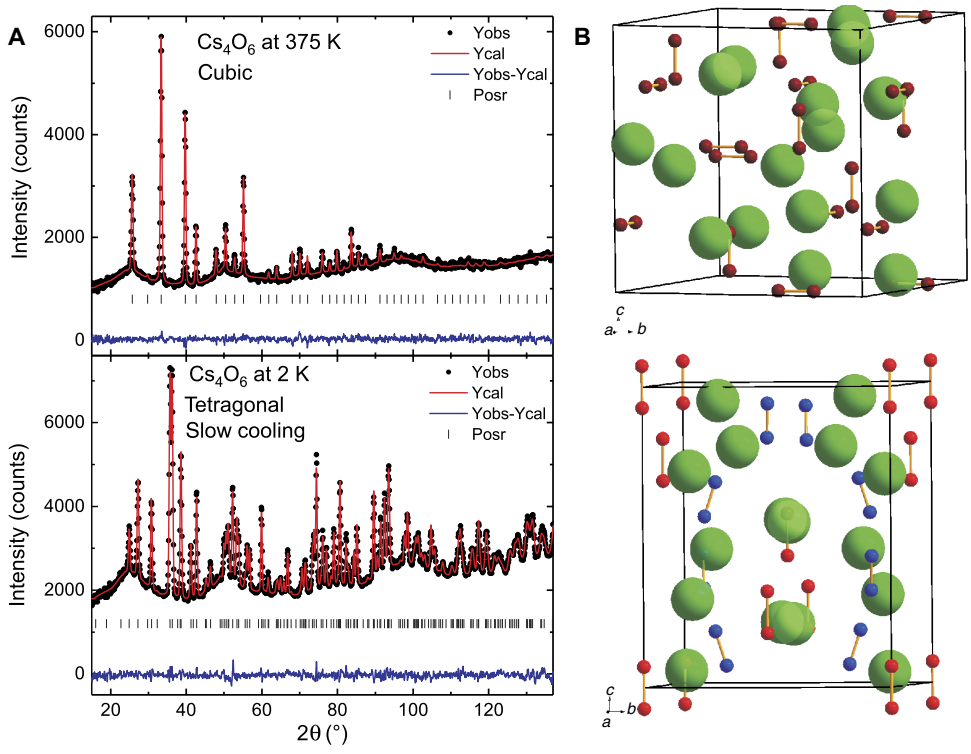

Fig. 1. Structural properties of Cs_4O_6. (**A**) Powder neutron diffraction patterns at 2 and 375 K. Top: At 375 K, Cs_4O_6 crystallizes in the C structure with space group $I\bar{4}3d$. Bottom: At 2 K, Cs_4O_6 crystallizes in the T structure with space group $I\bar{4}$. Black points and red and blue lines correspond to experimental data, calculated pattern, and difference curve, respectively. Broad humps in the patterns are due to the quartz tube containing the air-sensitive sample. (**B**) Illustration of the C (top) and T (bottom) crystal structures of Cs_4O_6. In the C structure, the O_2 units (brown) are indistinguishable, whereas the T structure features CO of distinct peroxide O_2^{2-} (red) and superoxide O_2^- (blue) anions. Cs^+ ions are shown as green spheres.

magnetic susceptibility (Fig. 2B, inset), where the structural transitions are reflected as anomalies (Fig. 2B), or with electron paramagnetic resonance (EPR) spectroscopy, where no critical broadening of the spectra or the characteristic antiferromagnetic resonance is observed down to 4 K (fig. S1).

From the temperature variation of lattice parameters (Fig. 2A), the fraction of the T phase (fig. S2A), and the magnetization (Fig. 2B), it is evident that on warming the C-T phase transition shows a pronounced hysteresis of about 50 K. This large hysteresis as well as the discontinuity in lattice parameters and cell volume (fig. S2B) point to a first-order phase transition, which is, in mixed-valence systems, one of the pertinent signatures of a Verwey-type transition. The anisotropic response of the lattice in the course of the C-T transition leads to a large decrease in unit cell volume by about 1.5%.

Because of on-site electron correlations and weak electronic overlap between neighboring O_2 entities, Cs_4O_6 adopts an insulating ground state (*13*). The Arrhenius plot of conductivity, σ, measured by impedance spectroscopy on a pressed pellet of Cs_4O_6 (Fig. 2C) reveals a thermally activated behavior and, concomitant with the structural transition from the C to T phase, a drop in σ by two orders of magnitude. The activation energies are virtually identical (~0.50 eV) for the C and T phase within the experimental errors. Upon completing the thermal cycle, the conductivities were the same for the cooling and heating branches of the measurement, respectively. The large structural hysteresis is reflected by a similarly broad hysteresis of σ between 313 and 233 K. In two control experiments conducted at a constant temperature of 273 K (during the cooling and then during the warming mode), conductivities remained nearly constant as a function of time for almost 3 days (fig. S3), proving that the observed hysteresis is not due to the slow kinetics of the phase transition. Because per formula unit one electron hops from O_2^{2-} to the nearest neighboring O_2^-, the charge carrier density amounts to 4 per unit cell volume (4 formula units per unit cell), which allows the calculation of the charge carrier mobility $u(T)$ as a function of temperature (fig. S4). For the C phase, one obtains $u(298\ K) \approx 10^{-9}$ cm^2/(V s) and, for the T phase, $u(213\ K) \approx 2 \times 10^{-15}$ cm^2/(V s). Applying the Nernst-Einstein relation, these mobility values correspond to charge carrier jump frequencies of $\omega(298\ K) \approx 1$ GHz and $\omega(213\ K) \approx 1.5$ kHz, respectively. Thus, the charge carrier dynamics in the C phase occurs on the nanosecond time scale, whereas it is slowed down considerably to the range of milliseconds in the T phase.

To follow the charge dynamics on a molecular level through the structural and CO transition, various complementary spectroscopies were used. The Raman spectrum of Cs_4O_6 at room temperature (Fig. 3) shows two distinct vibrational peaks corresponding to stretching vibrations of O_2^{2-} (767 cm^{-1}) and O_2^- (1139 cm^{-1}) species, thus proving charge localization on a time scale of 0.1 ps in the high-temperature C phase. This result compares well with a nanosecond time scale of the charge dynamics as derived from the impedance data (see Fig. 4A).

^{17}O (nuclear spin 5/2) nuclear magnetic resonance (NMR) spectra probe charge and molecular dynamics on a time scale of $\tau_{NMR} \sim 10^{-6}$ s. ^{17}O NMR spectra were measured on a sample of Cs_4O_6, which was enriched with the ^{17}O isotope. In the high-temperature C phase, enormous hyperfine fields at all O_2 sites, which are present because of the full charge delocalization on the τ_{NMR} scale [see table S3 for the compilation of the

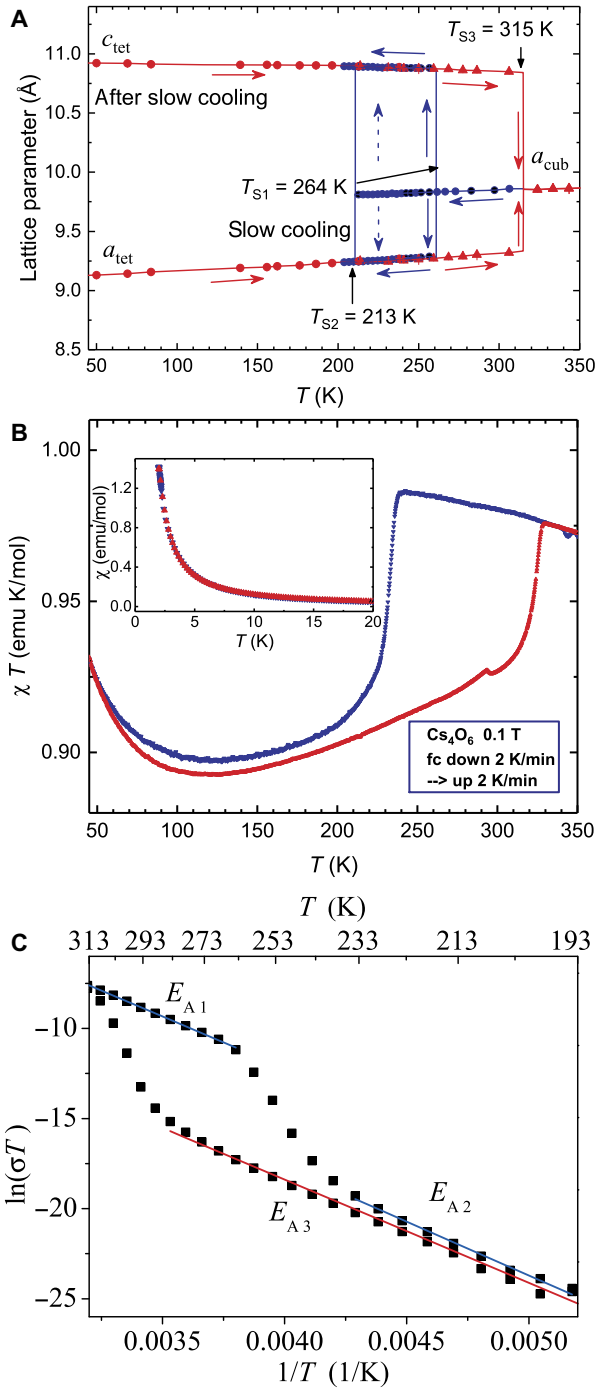

Fig. 2. Signatures of the Verwey-type transition in Cs_4O_6. (**A**) Temperature dependence of the lattice parameters a_{cub} of the C phase and a_{tet} and c_{tet} of the T phase. On cooling, the C to T transformation starts at T_{S1} = 264 K and is completed at T_{S2} = 213 K. On heating, transformation back into the C phase occurs near T_{S3} = 315 K. (**B**) The structural transition is reflected in anomalies and a hysteresis in the magnetic susceptibilities χ(*T*), as apparent in the representation of χ*T* versus *T*. The inset shows the low-temperature magnetic susceptibilities verifying the absence of long-range magnetic order down to 1.8 K. (**C**) Arrhenius plot of the conductivity of Cs_4O_6, featuring a hysteresis in the temperature range between 313 and 233 K. Blue and red lines are line fits for the determination of the activation energies E_{A1} to E_{A3}.

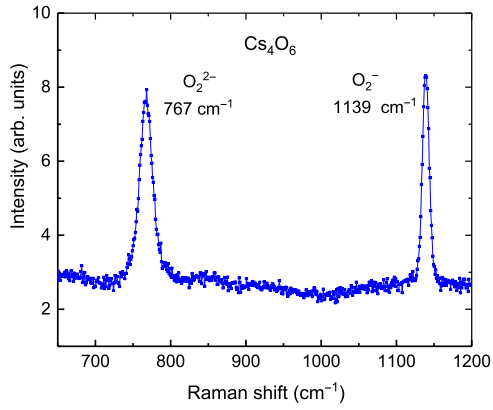

Fig. 3. Raman spectrum of Cs_4O_6 powder at room temperature. The vibrations at 767 and 1139 cm^{-1} correspond to the stretching vibrations of the peroxide and superoxide anions, respectively.

results from density functional theory (DFT) computations of hyperfine interactions and ^{17}O quadrupole frequencies], make any ^{17}O NMR signal unobservable (Fig. 4B, top). However, as the sample is cooled into the T phase, suddenly, a characteristic quadrupole powder line shape of the nuclear central transition $^1/_2 \leftrightarrow -^1/_2$ [Fig. 4B (bottom) and fig. S5] assigned solely to the closed-shell O_2^{2-} units emerges and unambiguously proves charge localization in the T phase (see the Supplementary Materials and fig. S6 for a detailed discussion of the line shape). Paramagnetic O_2^- units are not detectable in ^{17}O NMR due to the enormous hyperfine interaction between ^{17}O nuclear and the open-shell electronic moment (table S3). However, the latter are clearly observed as a broad line in X-band EPR spectra [Fig. 4C (bottom) and fig. S1]. In the C phase, due to a rapid hopping of charge comparable to the characteristic EPR time scale $\tau_{EPR} \sim 10^{-10}$ s, the broadening of the X-band EPR line is so large that the spectrum spans beyond the experimentally accessible field range (Fig. 4C, top). Thus, our two complementary magnetic resonance spectroscopy techniques further narrow down the time window for the charge dynamics in the high-temperature C phase to a range between $\sim 10^{-10}$ and 10^{-13} s, whereas in the low-temperature T phase it is between 10^{-6} and 10^{-3} s (Fig. 4A). During the CO, the wave function of the fourth electron, which extends over all O_2 dumbbells in the C phase, localizes on a single O_2 unit in the T phase (Fig. 4D).

DISCUSSION

Using various probes rendering different temporal and spatial resolutions has enabled us to establish the typical features of a Verwey-type transition in the open-shell *p*-electron compound Cs_4O_6, namely, a first-order structural transition from a charge-disordered into a charge-ordered phase and a concomitant drop in electronic conductivity, which is reflected in a corresponding drop in charge fluctuations rates (see Fig. 4A). Because of the large intermolecular distances, the electronic conductivities in both the charge-ordered and the charge-disordered phase of Cs_4O_6 are several orders of magnitude smaller than in Fe_3O_4, the canonical example for CO in 3*d* systems. Our spectroscopic investigations indicate for the high-temperature C phase charge delocalization on the NMR but charge localization on the vibrational time scale, which points to moderate electronic coupling between the

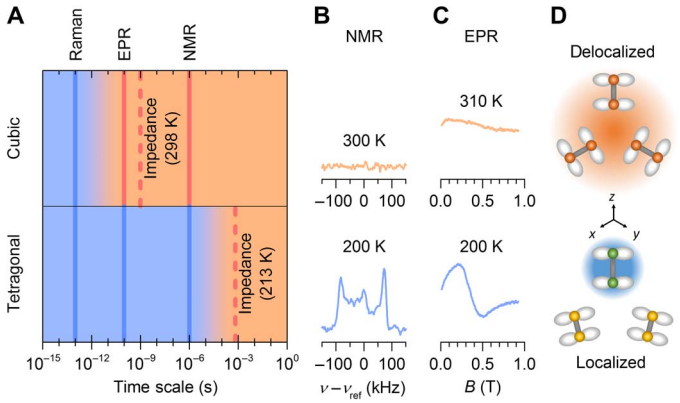

Fig. 4. Complementary spectroscopic techniques probe charge dynamics in the C and T phases of Cs_4O_6. (**A**) Sketch of characteristic time scales covered by the indicated experimental techniques. Orange and blue shading indicates the time scale range, where charge delocalization or localization is observed by respective spectroscopic probes. (**B**) Because of rapid charge exchange compared to τ_{NMR}, no ^{17}O NMR signal is observed in the C phase (top), whereas a quadrupole broadened powder spectrum due to nonmagnetic O_2^{2-} units is measured in the T phase (bottom). (**C**) Similarly, rapid charge exchange compared to τ_{EPR} dramatically broadens the X-band EPR spectrum in the C phase (top), whereas charge localization leads to a broad EPR signal in the T phase (bottom), corresponding to EPR active O_2^-. (**D**) Schematic picture of charge delocalization in the C phase (top), where the electronic wave function of the fourth electron (orange shaded area) extends over all three O_2 dumbbells in the formula unit. In the T phase (bottom), the extra electron localizes and its wave function (blue shaded area) shrinks to a single O_2^{2-} dumbbell, leaving the other two in the O_2^- paramagnetic state.

mixed-valence centers. Accordingly, Cs_4O_6 may be considered as a class II mixed-valence compound within the classification of Robin and Day (*1*). This implies the persistence of rapid charge fluctuations in the C phase of Cs_4O_6. Both structural and spectroscopic data verify that the low-temperature state of Cs_4O_6 is governed by complete CO of diamagnetic O_2^{2-} and paramagnetic O_2^- molecular anions, which is reminiscent of Verwey's original suggestion of simple ionic CO (Fe^{2+} and Fe^{3+} ions in the case of Fe_3O_4) (*3*). However, the true nature of the low-temperature state in Fe_3O_4 has been discussed controversially (*4*, *5*), and its CO pattern turned out to be much more complex than anticipated by Verwey. It involves the formation of a linear array of three Fe sites, so-called trimerons (*6*). Short-range correlations attributed to complexes of trimerons are believed to persist even above T_V (*27*).

The molecular nature of Cs_4O_6 offers the possibility to tackle fundamental questions on the mechanism of Verwey-type CO transitions, for instance, it may shed new light on the role played by orbital order, which was suggested to be a key feature for the formation of the complex CO state in Fe_3O_4 (*28*, *29*). In Cs_4O_6, an entanglement between charge and orbital order is expected because, in the electron-localized T CO phase, an intermolecular Jahn-Teller effect lifts the degeneracy of the partly occupied π^* molecular orbitals of the O_2^- entities by tilting them, which opens the path for orbital order to set in (*19*). An important role of orbital physics in the CO phase of Cs_4O_6 is revealed by the anomalous high-temperature broadening of the EPR spectra in the charge-ordered T phase (fig. S1B) (*30*). A large decrease in the unit cell volume at the C-T transition is a manifestation of unusually large coupling of the lattice to charge and orbital degrees of freedom, thus promoting Cs_4O_6 as particularly well suited for testing advanced concepts for Verwey-type CO transitions and exploring new physics beyond that available to the "standard" transition metal–based compounds.

MATERIALS AND METHODS

Sample preparation and characterization

Powders of Cs_4O_6 were prepared by thermal decomposition of CsO_2, as described in detail elsewhere (*31*). For ^{17}O NMR and EPR experiments, an isotopically enriched sample of Cs_4O_6 was synthesized along the same route starting with ^{17}O-enriched CsO_2. The latter was synthesized from Cs and $^{17}O_2$ gas (90% $^{17}O_2$; Sigma-Aldrich). The purity of the samples was checked by laboratory powder x-ray diffraction (XRD) measurements. Due to the extreme air and moisture sensitivity of alkali metal oxides, all sample handlings had to be carried out under carefully controlled inert atmospheres.

Powder neutron diffraction

For the PND experiments, powders of Cs_4O_6 (~4 g) were sealed in a thin-walled quartz tube, which was placed in a vanadium can. Measurements were carried out using the instruments E6 and E9 at the BER II reactor of the Helmholtz-Zentrum Berlin. A pyrolytic graphite and a Ge monochromator selected the neutron wavelengths $\lambda = 2.42$ Å (E6) and $\lambda = 1.7973$ Å (E9), respectively. Data were collected at the diffraction angles $8° \le 2\theta \le 136.5°$ on E6 and $8° \le 2\theta \le 141.8°$ on E9 in the temperature range between 1.6 and 375 K using a standard Orange cryostat and a cryo-furnace. Data from the high-resolution instrument E9 were used to precisely determine the positional parameters of the C and T structures, whereas the structural variations as a function of temperature were followed on E6. To reach a fully completed structural change of Cs_4O_6 from the high-temperature C to the low-temperature T phase, the sample was slowly cooled from 300 to 180 K, after heating up to 380 K, with a cooling rate of 0.5 K/min and subsequently with a cooling rate of ~3 K/min down to the base temperature. The changes of the structural properties of Cs_4O_6 were also followed with increasing temperature from 1.7 to 380 K, where the set temperature was always reached in about 10 min.

The refinements of the crystal structure were carried out with the program FullProf (*32*) with the nuclear scattering lengths $b(O) = 5.805$ fm and $b(Cs) = 5.42$ fm (*33*). All refinement results are summarized in table S1. The high-temperature C crystal structure of Cs_4O_6 was refined in space group $I\bar{4}3d$ (No. 220). The Cs and O atoms are located at the Wyckoff positions 16*c* (*x*,*x*,*x*) and 24*d* (x,0,$^3/_4$), respectively. The refinement of the positional parameters *x*(Cs) and *x*(O) and the two thermal parameters resulted in a somewhat enlarged residual $R_F = 0.155$ (defined as $R_F = \Sigma||F_{obs}| - |F_{calc}||/\Sigma|F_{obs}|$). This can be ascribed to the fact that the strongly enlarged thermal parameters lead to a strong decrease in intensity for the high-order Bragg reflections, as can be seen in Fig. 1A. However, the positional and thermal parameters could be determined with good accuracy. We note that anomalous temperature factors were also observed previously for the C phase of Rb_4O_6 (*24*, *25*).

The low-temperature T crystal structure of Cs_4O_6 was refined in space group $I\bar{4}$ (No. 82). Here, the Cs and O positions split into two and four atomic positions, respectively. Both atoms Cs1 and Cs2 occupy the Wyckoff position 8*g*(*x*,*y*,*z*), whereas the O atoms are located at the following positions: O1 at 4*e*(0,0,*z*), O2 at 4*f*($0,^1/_2,z$), and both O3 and O4 at 8*g*(*x*,*y*,*z*). From the Rietveld refinement of the PND pattern collected at 2 K, we have obtained a satisfactory residual $R_F = 0.0326$

(χ^2 = 1.65). Interatomic distances obtained from the evaluation of the PND data of the T phase at 2 K are summarized in table S2.

Impedance measurements

Cs_4O_6 pellets with a diameter of 6 mm and a thickness of around 1 mm were pressed for impedance measurements. Gold foil with a diameter of 6 mm was fixed as electrodes to the two sides of the Cs_4O_6 pellets. The pellets were connected with nickel tabs as current collectors and were sealed in gas-tight pouch foil in an argon-filled glove box [MBRAUN, <0.1 parts per million (ppm) H_2O, <0.1 ppm O_2]. Temperature-dependent impedance measurements were then carried out using an Alpha-A mainframe by Novocontrol Technologies with an equipped POT/GAL30V2A electrochemical test station and a ZG4 test interface.

The measurements were carried out in a temperature range of 313 to 173 K in steps of 5 K. The temperature was adjusted using a liquid nitrogen–based cooling system and a heating coil. The sample holder was placed in a steel vessel, where it was cooled in the nitrogen gas flow. For each temperature step, a relaxation time of 2.5 hours was chosen with a maximum temperature change of 0.3 K/min. The impedance was measured between 10 MHz and 10 mHz with a sinus amplitude of 10 mV. Data evaluation was performed using the software RelaxIS 3 (rhd instruments).

For fitting the data, an equivalent circuit consisting of a parallel resistor R and a constant phase element Q was chosen because neither the Nyquist nor the Bode plot indicated the presence of more than one charge transport process. From the resulting resistances and the diameter and thickness of the sample, temperature-dependent conductivities σ were calculated.

To determine whether the hysteresis in σ was due to the slow kinetics of the phase transition, additional measurements were carried out. The impedance was measured for 500 full frequency cycles (the corresponding total measurement time is about ~3 days) at a constant temperature of 273 K (fig. S3). One measurement was performed after cooling the sample from 313 to 273 K, maintaining the C structure; the other measurement was performed after approaching 273 from 173 K, thus keeping the T structure.

The conductivity of the C structure at 273 K was determined as 6.9×10^{-8} S cm^{-1} and remained at this value for more than 500 full frequency cycles (~3 days). The slight decay of the conductivity in the first 10 cycles was due to reaching thermal equilibrium that had not been established yet.

The conductivity of the T structure was determined as 4.1×10^{-10} S cm^{-1} and remained constant for 3 days. Again, the slight deviation from this value during the first measurement cycles is attributed to the establishment of thermal equilibrium. The constant conductivity of the T phase at 273 K indicated the stability of the T structure, which did not transform into the C structure even after 3 days.

Assuming a charge carrier density n of $4/V_{cell}$ (V_{cell} represents the unit cell volume as determined by XRD), we obtained the electron mobility as a function of temperature (fig. S4) from the electronic conductivity σ_{el} according to $u = \frac{\sigma_{el}}{e_0 \cdot n}$ with the electron charge e_0 and the charge carrier density n. Because the electron concentration changes only due to the thermal lattice expansion, the dramatic jump in conductivity directly represents a jump of the electron mobility. The diffusion coefficient D of the electrons is calculated using the Nernst-Einstein relation $D = \frac{u \cdot k_B T}{e_0}$ with the Boltzmann constant k_B and the absolute temperature T. Assuming isotropic diffusion of the electrons, the diffusion coefficient D is related to the jump distance a and the jump frequency ω according to $D = \frac{1}{6} \cdot a^2 \cdot \omega$. For the jump distance a, the shortest intermolecular O–O distance of 390 pm was used.

Raman spectroscopy

Raman spectra of Cs_4O_6 sealed in a quartz capillary were taken at room temperature with a Jobin Yvon LabRAM V 010 single-grating spectrometer, equipped with a double super razor edge filter and a Peltier-cooled charge-coupled device camera. The resolution of the spectrometer (grating 1800 L/mm) is 1 wave number (cm^{-1}). The spectra were taken in quasi-backscattering geometry using the linearly polarized 632.8-nm line of a He/Ne gas laser. A small laser power of 0.4 mW was used as spectral changes in the region of the O_2^{2-} vibration were observed at higher laser power. The spot size was 10 μm.

Magnetization measurements

Magnetization measurements on powders of Cs_4O_6 sealed in a Suprasil quartz tube were performed with an MPMS3 (Quantum Design) magnetometer in field-cooling and field-heating modes in a magnetic field of 0.1 T. Starting from 350 K, the sample was cooled with a rate of 2 K/min down to 2 K and subsequently heated back to 350 K at the same rate.

EPR spectroscopy

For the EPR measurements, around 5 mg of ^{17}O-enriched Cs_4O_6 powder was sealed under dynamic vacuum in a standard Suprasil quartz tube. Continuous wave X-band EPR spectra were measured on a homebuilt spectrometer equipped with a Varian E-101 microwave bridge, a Varian TEM104 dual-cavity resonator, an Oxford Instruments ESR900 cryostat, and an Oxford Instruments ITC503 temperature controller. The temperature stability was better than ±0.05 K at all temperatures.

The EPR spectra (fig. S1A) were measured during cooling and warming up the sample. The sample was cooled from 325 to 4 K in 24 hours with a constant rate of 0.22 K/min, whereas the average warming up rate was about 0.5 K/min. The powder X-band EPR spectra were observed clearly only in the T phase, in agreement with our previous report (*20*). The temperature dependence of the EPR linewidth and the intensity of the EPR signal are presented in fig. S1, B and C, respectively.

^{17}O NMR spectroscopy

^{17}O (nuclear spin I = 5/2) NMR spectra were measured for the ^{17}O-enriched sample of Cs_4O_6 between 4 and 325 K at a magnetic field of 9.39 T. As a reference, the ^{17}O NMR signal from H_2O was used with the corresponding reference frequency $\nu_{ref}(^{17}O)$ = 54.227 MHz. Because the ^{133}Cs (nuclear spin I = 7/2) NMR signal is very close to the ^{17}O NMR resonance [the reference compound $CsNO_3$ has a reference frequency $\nu_{ref}(^{133}Cs)$ = 52.461 MHz], the ^{133}Cs NMR signal was simultaneously detected in wide frequency sweeps. In the ^{17}O NMR experiments, a two-pulse solid-echo sequence (β)-τ-(β)-τ was used with a pulse length, $\tau_w(\beta)$ = 7 μs, optimized to the ^{17}O NMR signal, and an interpulse delay τ = 50 μs. The complete polycrystalline NMR spectra (fig. S6) were obtained by summing the real part of spectra measured at different frequencies separated by δν = 50 kHz. To convert the C into the T phase, the sample was cooled from 325 to 50 K in 20 hours at a cooling rate of 0.23 K/min.

To correctly simulate the entire powder ^{17}O NMR spectrum, the quadrupole interaction was included in perturbation theory up to the second order for both the central and the satellite transitions.

The quadrupole shift of the $m \leftrightarrow m-1$ nuclear transition in the ith order is $\nu_Q^i(m,\vartheta,\varphi) = \frac{1}{h}(E^{(i)}(I,m,\vartheta,\varphi) - E^{(i)}(I,m-1,\vartheta,\varphi))$. Here, ϑ and φ are the polar and the azimuthal angles of the magnetic field orientation with respect to the principal coordinate system of the quadrupole interaction. The expressions for the first- and second-order quadrupole energies $E^{(i)}(I,m,\vartheta,\varphi)$ can be found in the study of Potočnik *et al.* (*34*). In calculations of powder NMR spectra, initially, a uniform distribution of cos ϑ and φ has been assumed. However, an additional narrow peak appeared in the center of the ^{17}O NMR spectra (fig. S6) when the powder sample was cooled into the T phase. This peak is attributed to those grains in the T phase, which oriented in the strong external magnetic field due to considerable magnetic anisotropy. Therefore, to account for this peak, a nonuniform distribution in the grain orientation with a narrow peak at $\vartheta = 0$ has been assumed. The same parameters of the quadrupole Hamiltonian, the quadrupole frequency $\nu_Q = 2.6$ MHz and the asymmetry $\eta = 0.09$, were used for the oriented and uniformly distributed (nonoriented) part of the sample. For the presented set of measurements, we found that around 10% of the powder grains oriented with a T c axis parallel to the magnetic field at $T = 50$ K. We stress that the orientation of crystallites in a strong magnetic field is not entirely unexpected and has been observed before in other systems, for example, in the study of Haarmann *et al.* (*35*).

First-principle computations of NMR parameters

The hyperfine coupling constants and quadrupole frequencies were calculated ab initio within the framework of the DFT by applying the QUANTUM ESPRESSO code (*36*). The exchange-correlation effects were calculated by means of the generalized gradient approximation (*37*) with explicitly added (*38*) Hubbard repulsion term $U = 4.1$ eV for the oxygen atoms. The electron-ion interactions were described with the gauge-including projected augmented wave (GIPAW) pseudopotentials (*39*), making it possible to calculate the NMR-based quantities. The plane waves and the charge-density cutoff parameters were set to 639 and 2543 eV, respectively, whereas a $4 \times 4 \times 4$ mesh of k points (*40*) was used for the Brillouin zone integration. The self-consistent criterion was the total energy difference between the two subsequent calculations being less than 10^{-6} Ry.

In the computations of the ^{17}O NMR parameters for the C and T phase, we used the structural parameters extracted from the PND data at 320 and 2 K, respectively. The eigenvalues of the electric field gradient components V_{xx}, V_{yy}, and V_{zz} and of the ^{17}O contact (Fermi) hyperfine field A (expressed in the units of MHz) are summarized in table S3.

SUPPLEMENTARY MATERIALS

Supplementary material for this article is available at http://advances.sciencemag.org/cgi/content/full/4/1/eaap7581/DC1

section S1. Temperature dependence of the X-band EPR spectra
section S2. ^{17}O NMR line shape modeling
section S3. Temperature dependence of the ^{17}O NMR spectra
fig. S1. X-band EPR spectra of Cs_4O_6 for selected temperatures.
fig. S2. Structural phase transition in Cs_4O_6.
fig. S3. Time-dependent conductivity of a Cs_4O_6 pellet at 273 K.
fig. S4. Temperature dependence of the charge carrier mobility for Cs_4O_6.
fig. S5. Temperature dependence of the powder central transition ^{17}O NMR spectra.
fig. S6. Line shape modeling of powder ^{17}O NMR spectrum of isotopically enriched Cs_4O_6.
table S1. Results of the crystal structure refinements of Cs_4O_6 from PND data.
table S2. Interatomic distances (in Å) as obtained from the crystal structure refinements of Cs_4O_6 PND data at 2 K.
table S3. Results from DFT calculations.

REFERENCES AND NOTES

1. M. B. Robin, P. Day, Mixed valence chemistry—A survey and classification. *Adv. Inorg. Chem. Radiochem.* **10**, 247–422 (1967).
2. E. J. W. Verwey, Electronic conduction of magnetite (Fe_3O_4) and its transition point at low temperatures. *Nature* **144**, 327–328 (1939).
3. E. J. Verwey, P. W. Haayman, F. C. Romeijn, Physical properties and cation arrangement of oxides with spinel structures. II. Electronic conductivity. *J. Chem. Phys.* **15**, 181–187 (1947).
4. F. Walz, The Verwey transition—A topical review. *J. Phys. Condens. Matter* **14**, R285–R340 (2002).
5. J. García, G. Subías, The Verwey transition—A new perspective. *J. Phys. Condens. Matter* **16**, R145–R178 (2004).
6. M. S. Senn, J. P. Wright, J. P. Attfield, Charge order and three-site distortions in the Verwey structure of magnetite. *Nature* **481**, 173–176 (2012).
7. C. N. R. Rao, B. Raveau, Eds., *Colossal Magnetoresistance, Charge Ordering and Related Properties of Manganese Oxides*, (World Scientific Publishing, 1998).
8. M. Uehara, S. Mori, C. H. Chen, S.-W. Cheong, Percolative phase separation underlies colossal magnetoresistance in mixed-valent manganites. *Nature* **399**, 560–563 (1999).
9. M. B. Salamon, M. Jaime, The physics of manganites: Structure and transport. *Rev. Mod. Phys.* **73**, 583–628 (2001).
10. J. Chang, E. Blackburn, A. T. Holmes, N. B. Christensen, J. Larsen, J. Mesot, R. Liang, D. A. Bonn, W. N. Hardy, A. Watenphul, M. v. Zimmermann, E. M. Forgan, S. M. Hayden, Direct observation of competition between superconductivity and charge density wave order in $YBa_2Cu_3O_{6.67}$. *Nat. Phys.* **8**, 871–876 (2012).
11. E. H. da Silva Neto, P. Aynajian, A. Frano, R. Comin, E. Schierle, E. Weschke, A. Gyenis, J. Wen, J. Schneeloch, Z. Xu, S. Ono, G. Gu, M. Le Tacon, A. Yazdani, Ubiquitous interplay between charge ordering and high temperature superconductivity in cuprates. *Science* **343**, 393–396 (2014).
12. P. Horsch, M. Sofin, M. Mayr, M. Jansen, Wigner crystallization in $Na_3Cu_2O_4$ and $Na_8Cu_5O_{10}$ chain compounds. *Phys. Rev. Lett.* **94**, 76403 (2005).
13. J. Winterlik, G. H. Fecher, C. A. Jenkins, C. Felser, C. Mühle, K. Doll, M. Jansen, L. M. Sandratskii, J. Kübler, Challenge of magnetism in strongly correlated open-shell 2*p* systems. *Phys. Rev. Lett.* **102**, 16401 (2009).
14. J. Winterlik, G. H. Fecher, C. A. Jenkins, S. Medvedev, C. Felser, J. Kübler, C. Mühle, K. Doll, M. Jansen, T. Palasyuk, I. Trojan, M. I. Eremets, F. Emmerling, Exotic magnetism in the alkali sesquioxides Rb_4O_6 and Cs_4O_6. *Phys. Rev. B* **79**, 214410 (2009).
15. I. V. Solovyev, Spin-orbital superexchange physics emerging from interacting oxygen molecules in KO_2. *New J. Phys.* **10**, 013035 (2008).
16. O. Volnianska, P. Boguslawski, Magnetism of solids resulting from spin polarization of *p* orbitals. *J. Phys. Condens. Matter* **22**, 073202 (2010).
17. E. R. Ylvisaker, R. R. P. Singh, W. E. Pickett, Orbital order, stacking defects, and spin fluctuations in the *p*-electron molecular solid RbO_2. *Phys. Rev. B* **81**, 180405(R) (2010).
18. K. Wohlfeld, M. Daghofer, A. M. Oleś, Spin-orbital physics for *p* orbitals in alkali RO_2 hyperoxides—Generalization of the Goodenough-Kanamori rules. *Eurphys. Lett.* **96**, 27001 (2011).
19. S. Riyadi, B. Zhang, R. A. de Groot, A. Caretta, P. H. M. van Loosdrecht, T. T. M. Palstra, G. R. Blake, Antiferromagnetic *S*=1/2 spin chain driven by *p*-orbital ordering in CsO_2. *Phys. Rev. Lett.* **108**, 217206 (2012).
20. D. Arčon, K. Anderle, M. Klanjšek, A. Sans, C. Mühle, P. Adler, W. Schnelle, M. Jansen, C. Felser, Influence of O_2 molecular orientation on *p*-orbital ordering and exchange pathways in Cs_4O_6. *Phys. Rev. B* **88**, 224409 (2013).
21. M. Klanjšek, D. Arčon, A. Sans, P. Adler, M. Jansen, C. Felser, Phonon-modulated magnetic interactions and spin Tomonaga-Luttinger liquid in the *p*-orbital antiferromagnet CsO_2. *Phys. Rev. Lett.* **115**, 057205 (2015).
22. T. Knaflič, M. Klanjšek, A. Sans, P. Adler, M. Jansen, C. Felser, D. Arčon, One-dimensional quantum antiferromagnetism in the *p*-orbital CsO_2 compound revealed by electron paramagnetic resonance. *Phys. Rev. B* **91**, 174419 (2015).
23. A. Helms, W. Klemm, Über die Kristallstrukturen der Rubidium- und Cäsiumsesquioxyde. *Z. Anorg. Allg. Chem.* **242**, 201–214 (1939).
24. M. Jansen, N. Korber, Neue Untersuchungen zu Präparation und Struktur von Rb_4O_6. *Z. Anorg. Allg. Chem.* **598**, 163–173 (1991).
25. M. Jansen, R. Hagenmayer, N. Korber, Rb_4O_6 studied by elastic and inelastic neutron scattering: In memoriam Jean Rouxel. *C. R. Acad. Sci. Ser.* **2**, 591–594 (1999).
26. A. Sans, J. Nuss, G. H. Fecher, C. Mühle, C. Felser, M. Jansen, Structural implications of spin, charge, and orbital ordering in rubidium sesquioxide, Rb_4O_6. *Z. Anorg. Allg. Chem.* **640**, 1239–1246 (2014).
27. A. Bosak, D. Chernyshov, M. Hoesch, P. Piekarz, M. Le Tacon, M. Krisch, A. Kosłowski, A. M. Olès, K. Parlinski, Short-range correlations in magnetite above the Verwey temperature. *Phys. Rev. X* **4**, 011040 (2014).
28. H.-T. Jeng, G. Y. Guo, D. J. Huang, Charge-orbital ordering and Verwey transition in magnetite. *Phys. Rev. Lett.* **93**, 156403 (2004).

29. J. Schlappa, C. Schüßler-Langeheine, C. F. Chang, H. Ott, A. Tanaka, Z. Hu, M. W. Haverkort, E. Schierle, E. Weschke, G. Kaindl, L. H. Tjeng, Direct observation of t_{2g} orbital ordering in magnetite. *Phys. Rev. Lett.* **100**, 026406 (2008).
30. Z. Wang, M. Schmidt, A. Günther, S. Schaile, N. Pascher, F. Mayr, Y. Goncharov, D. L. Qintero-Castro, A. T. M. N. Islam, B. Lake, H.-A. Krug von Nidda, A. Loidl, J. Deisenhofer, Orbital fluctuations and orbital order below the Jahn-Teller transition in $Sr_3Cr_2O_8$. *Phys. Rev. B* **83**, 201102(R) (2011).
31. P. Merz, M. Schmidt, C. Felser, M. Jansen, Thermo-analytical investigations on the superoxides AO_2 (A = K, Rb, Cs), revealing facile access to sesquioxides A_4O_6. *Z. Anorg. Allg. Chem.* **643**, 544–547 (2017).
32. J. Rodríguez-Carvajal, Recent advances in magnetic structure determination by neutron powder diffraction. *Phys. B Condens. Matter* **192**, 55–69 (1993).
33. V. F. Sears, *International Tables for Crystallography*, A. J. C. Wilson, Ed. (Kluwer Academic Publishers, 1995), vol. C, p. 383.
34. A. Potočnik, P. Jeglič, K. Kobayashi, K. Kawashima, S. Kuchida, J. Akimitsu, D. Arčon, Anomalous local spin susceptibilities in noncentrosymmetric La_2C_3 superconductor. *Phys. Rev. B* **90**, 104507 (2014).
35. F. Haarmann, K. Koch, D. Grüner, W. Schnelle, O. Pecher, R. Cardoso-Gil, H. Borrmann, H. Rosner, Y. Grin, Electronic structure, chemical bonding and solid-state NMR spectroscopy of the digallides of Ca, Sr, and Ba. *Chem. Eur. J.* **15**, 1673–1684 (2009).
36. P. Giannozzi, S. Baroni, N. Bonini, M. Calandra, R. Car, C. Cavazzoni, D. Ceresoli, G. L. Chiarotti, M. Cococcioni, I. Dabo, A. Dal Corso, S. de Gironcoli, S. Fabris, G. Fratesi, R. Gebauer, U. Gerstmann, C. Gougoussis, A. Kokalj, M. Lazzeri, L. Martin-Samos, N. Marzari, F. Mauri, R. Mazzarello, S. Paolini, A. Pasquarello, L. Paulatto, C. Sbraccia, S. Scandolo, G. Sclauzero, A. P. Seitsonen, A. Smogunov, P. Umari, R. M. Wentzcovitch, QUANTUM ESPRESSO: A modular and open-source software project for quantum simulations of materials. *J. Phys. Condens. Matter* **21**, 395502 (2009).
37. J. P. Perdew, K. Burke, M. Ernzerhof, Generalized gradient approximation made simple. *Phys. Rev. Lett.* **77**, 3865–3868 (1996).
38. M. Cococcioni, S. de Gironcoli, Linear response approach to the calculation of the effective interaction parameters in the LDA + U method. *Phys. Rev. B* **71**, 035105 (2005).
39. C. J. Pickard, F. Mauri, All-electron magnetic response with pseudopotentials: NMR chemical shifts. *Phys. Rev. B* **63**, 245101 (2001).
40. H. J. Monkhorst, J. D. Pack, Special points for Brillouin-zone integrations. *Phys. Rev. B* **13**, 5188–5192 (1976).

Acknowledgments: We thank W. Schnelle and R. Koban for performing magnetization measurements and A. Schulz and P. Naumov for measuring Raman spectra. **Funding:** This project was supported by the European Union FP7-NMP-2011-EU-Japan project LEMSUPER under contract no. 283214. Fruitful discussions at the LEMSUPER consortium meetings are acknowledged. P.J., T.K., and D.A. acknowledge the financial support from the Slowenien Research Agency (core research funding number P1-0125). **Author contributions:** P.A., D.A., and M.J. coordinated the project and wrote the manuscript with contributions from the other authors. C.F. initiated and supervised the project. P.M. and A.S. synthesized samples. M.R., M.J., and P.A. planned and discussed the PND experiments, which were performed by M.R. and A.H. The impedance measurements were performed and evaluated by M.G. and J.J. The EPR and NMR spectra were measured and evaluated by P.J., T.K., and D.A. The DFT calculations were performed by M.K. All authors contributed to scientific discussions of the results. **Competing interests:** The authors declare that they have no competing interests. **Data and materials availability:** All data needed to evaluate the conclusions in the paper are present in the paper and/or the Supplementary Materials. Additional data related to this paper may be requested from the corresponding authors (M.J. or D.A.).

Submitted 23 August 2017
Accepted 11 December 2017
Published 19 January 2018
10.1126/sciadv.aap7581

Citation: P. Adler, P. Jeglič, M. Reehuis, M. Geiß, P. Merz, T. Knaflič, M. Komelj, A. Hoser, A. Sans, J. Janek, D. Arčon, M. Jansen, C. Felser, Verwey-type charge ordering transition in an open-shell *p*-electron compound. *Sci. Adv.* **4**, eaap7581 (2018).

Verwey-type charge ordering transition in an open-shell *p*-electron compound

Peter Adler, Peter Jeglic, Manfred Reehuis, Matthias Geiß, Patrick Merz, Tilen Knaflic, Matej Komelj, Andreas Hoser, Annette Sans, Jürgen Janek, Denis Arcon, Martin Jansen and Claudia Felser

Sci Adv **4** (1), eaap7581.
DOI: 10.1126/sciadv.aap7581